On the VOF Simulation Details and Droplet Size Distribution inside Rotating Packed Beds

Shahab Golshan[1,2], Roshanak Rabiee[2], Alireza Shams[2], Rayane Hoballah[3], Priyank Maheshwari[4], Rouzbeh Jafari[2], Jamal Chaouki[2], Bruno Blais[1*]

[1]Research Unit for Industrial Flows Processes (URPEI), Department of Chemical Engineering, École Polytechique de Montréal, PO Box 6079, Stn Centre-Ville, Montréal, QC, Canada H3C 3A7

[2]Process Engineering Advanced Research Lab (PEARL), Department of Chemical Engineering, École Polytechique de Montréal, PO Box 6079, Stn Centre-Ville, Montréal, QC, Canada H3C 3A7

[3]TOTAL Research Center CSTJF

[4]TOTAL Research Center Qatar

Abstract

In this research, the Volume of Fluid (VOF) method is used to study the hydrodynamics of rotating packed beds. The model is validated, and grid dependency analyses are performed for cases with different operating conditions. The droplet size distribution is investigated to characterize the hydrodynamics of rotating packed beds. Droplet size distributions are compared in two-dimensional and three-dimensional simulations, and it is demonstrated that two-dimensional simulations could provide an accurate prediction while significantly reducing

* Corresponding author:
Bruno Blais : Bruno.blais@polymtl.ca

significant computational cost. Radial distributions of droplet diameter in the packing region are studied, and different trends are observed at different rotational speeds (fluctuating at ω=250 rpm, increasing-constant at ω=500 rpm, and decreasing at higher rotational speeds). These trends are explained using the breakup and coalescence of droplets during droplet-packing and droplet-droplet collisions. Breakup, coalescence, and deposition regimes of droplets depend on the Weber, Ohnesorge, and impact parameter. We observed that with increasing rotational speed, the average droplet diameter and its standard deviation decreased while changing the liquid flow rate did not significantly affect the average droplet diameter. It is also observed that there is critical rotational speed (depending on the bed configuration), beyond which average droplet size does not decrease with increasing rotational speed.

Keywords: Rotating packed bed, CO_2 capture, Droplet size distribution, Droplet breakup and coalescence, Volume of fluid

1. Introduction

According to the Intergovernmental Panel on Climate Change (IPCC), before 2050, emissions of greenhouse gasses will increase the average global temperature by 1.1 to 2 ^oC [1, 2]. As reported by NASA (NASA, 2020), the average temperature of the planet has risen about 1.14 ^oC since the late 19th century, a change driven mainly by increased carbon dioxide emissions [3]. Most of the warming occurred in the past 35 years, with the six warmest years on record taking place since 2014 [3]. An increase of 2 ^oC in global average temperature will lead to irrecoverable consequences, and IPCC has therefore stated that global CO_2 emissions must be reduced by 50 to 80 percent by 2050 [1]. Despite this, the world is dangerously off-track. Even by considering

abrupt traumatic events like the Coronavirus pandemic, it is expected that the world economy is set to double in the next twenty years. Consequently, it is inevitable to apply new efficient and operational solutions to improve the applicability and efficiency of carbon-capture processes. Rotating packed beds (RPB) are an interestsing unit operation that could enable efficient carbon-capture..

Rotating packed beds are multiphase gas-liquid contactors/reactors presented for the first time by Ramshaw and Mallinson [4, 5]. Due to continuous renewing of the gas-liquid interface, RPBs provide promising intensification to the mass transfer compared to conventional packed beds [6-8]. Current applications of RPB reactors include post-combustion CO_2 capture [9-13], wastewater treatment [14], ozone oxidation [15], synthesis of nanoparticles [16], and distillation [17-18]. In a RPB, the liquid that is radially injected into the bed through an inlet located in the center of the reactor, collides with a packing rotating at an extremely high speed and splits into films, filaments, and finally tiny droplets [19]. Although several packing configurations have been proposed for RPBs [19], the most utilized packing types are wire mesh and Nickel foam packing [20, 21]. Despite a remarkable mass transfer enhancement, the extremely complex hydrodynamic of these beds has not been thoroughly studied [6, 10, 22].

Table 1. Some of the recent experimental and modeling studies of RPBs.

Ref.	Method	Major remarks
[20]	Experimental, X-ray CT scanner	• The distribution of liquid in the RPB is improved by increasing the rotating speed • Increasing rotational speed and decreasing liquid flow rate and liquid viscosity, decreased the liquid holdup

		• Using surfactants did not have significant effect on the liquid holdup • By increasing the rotational speed from 500 to 1000 rpm, liquid holdup decreased significantly and by further increase of the rotational speed, it decreased gradually • Wire mesh packing produced stronger shear stress and smaller droplets, compared to Nickel foam packing
[29, 30]	Experimental, High-speed camera	• Liquid flow pattern, impaction-disintegration modes of droplet-packing interaction, droplet velocity and size were investigated • A semi-empirical model of droplet velocity was proposed • Average droplet size decreased with increasing the rotational velocity, while increasing the liquid flow rate (i.e. liquid velocity) did not have significant effect on it
[19]	Experimental, Sampling from gas and liquid	• Effect of wire mesh packing with different structures and cross-sectional areas were investigated on the gas-liquid mass transfer • Compared with coiled wire mesh packing, concentric wire mesh packing with constant cross-sectional area showed higher effective interfacial area and volumetric mass transfer coefficient
[6]	Experimental and CFD,	• A correlation was proposed for prediction of average droplet diameter • Formation of droplets was mainly attributed to combination of liquid surface tension and centrifugal force

	Charged-coupled device camera, VOF	• Generally, average diameter of the droplets decreased with increasing the rotational speed; and as the rotational speed increases, the decreasing trend becomes slower • Average droplet diameter increased with increasing the inlet liquid velocity
[27, 28]	Experimental and CFD, High-speed photography, VOF and Eulerian method	• RPB with Nickel foam packing was simulated using VOF and Eulerian CFD models • X-ray computed micro-tomography (CT) was used to obtain the structure of the Nickel foam packing • A correlation was proposed to predict the volumetric liquid percentage of liquid droplets • Average droplet diameter did not show any dependence on the inlet liquid velocity • Average droplet velocity at the outer cavity zone linearly increased with increasing the rotational speed
[23, 24]	CFD, Eulerian method using a porous media model	• An Eulerian method with a porous media model was proposed and implemented to model large-scale RPBs • A modified porous media model is proposed for RPBs • With increasing the rotation speed, the overall gas phase mass transfer coefficient increased
[25]	CFD, Meso-scale VOF-based model	• A 3D meso-scale CFD model is proposed to simulate RPBs • New correlations were proposed to predict liquid holdup, specific surface area and interfacial area

		• With increasing the rotational speed, liquid holdup decreased and the specific surface area increased, while the effective interfacial area showed a weak positive dependency on the rotation speed • With increasing the liquid flow rate and/or liquid viscosity, liquid holdup and effective interfacial area increased
[10]	CFD, VOF	• With increasing the rotational speed, the liquid holdup decreased and the liquid dispersion increased • With increasing the liquid inlet velocity, the liquid holdup slightly increased • With increasing the Monoethanolamine (MEA) concentration, the liquid holdup increased and liquid dispersion degree decreased • It is very difficult to study the details of gas and liquid flow, without resolving the packing geometry in the CFD simulation • The packing region can be divided into two main zones: entrance and bulk regions; in the entrance region, the radial velocity of the liquid decreased from the jet velocity, while the tangential velocity increased from zero to the tangential velocity of the packing; in the bulk region, pore-dominant and droplet-dominant flow patterns were observed at low and high rotational velocities, respectively • A small percentage of the liquid adhered to the wire packing mesh and rotated with the packing

[22]	CFD, VOF	• Effects of nozzle (liquid inlet) configuration, including the number of nozzles and width of the nozzles, were studied on the performance of RPB • It was observed that increasing the number of nozzles and nozzle width increase the liquid holdup • With increasing the number of nozzles and decreasing the width of the nozzle, the circumferential distribution of the liquid became more uniform

Hydrodynamics of RPBs can be studied employing experimental and modeling methods [19-30]. In Table 1, some of the recent experimental and modeling research on the study of the hydrodynamics of RPBs are reported. As can be observed in Table 1, experimental methods in the study of the hydrodynamics of RPBs mainly include sampling from the inlet and outlet gas and liquid streams, high-speed camera, and X-ray computed tomography (CT) scanning [6, 19, 20, 27-30]. Two main approaches have been generally utilized in the literature on the modeling side: compartmental modeling and computational fluid dynamics (CFD). In compartmental modeling, the reactor is divided into different zones and in each zone, the equations of conservation for mass and energy, coupled with equations for interphase heat and mass transfer, are solved [31]. In the CFD simulations, different moldeing approaches based on meso or micro-scales were implemented and are summarized in Figure 1.

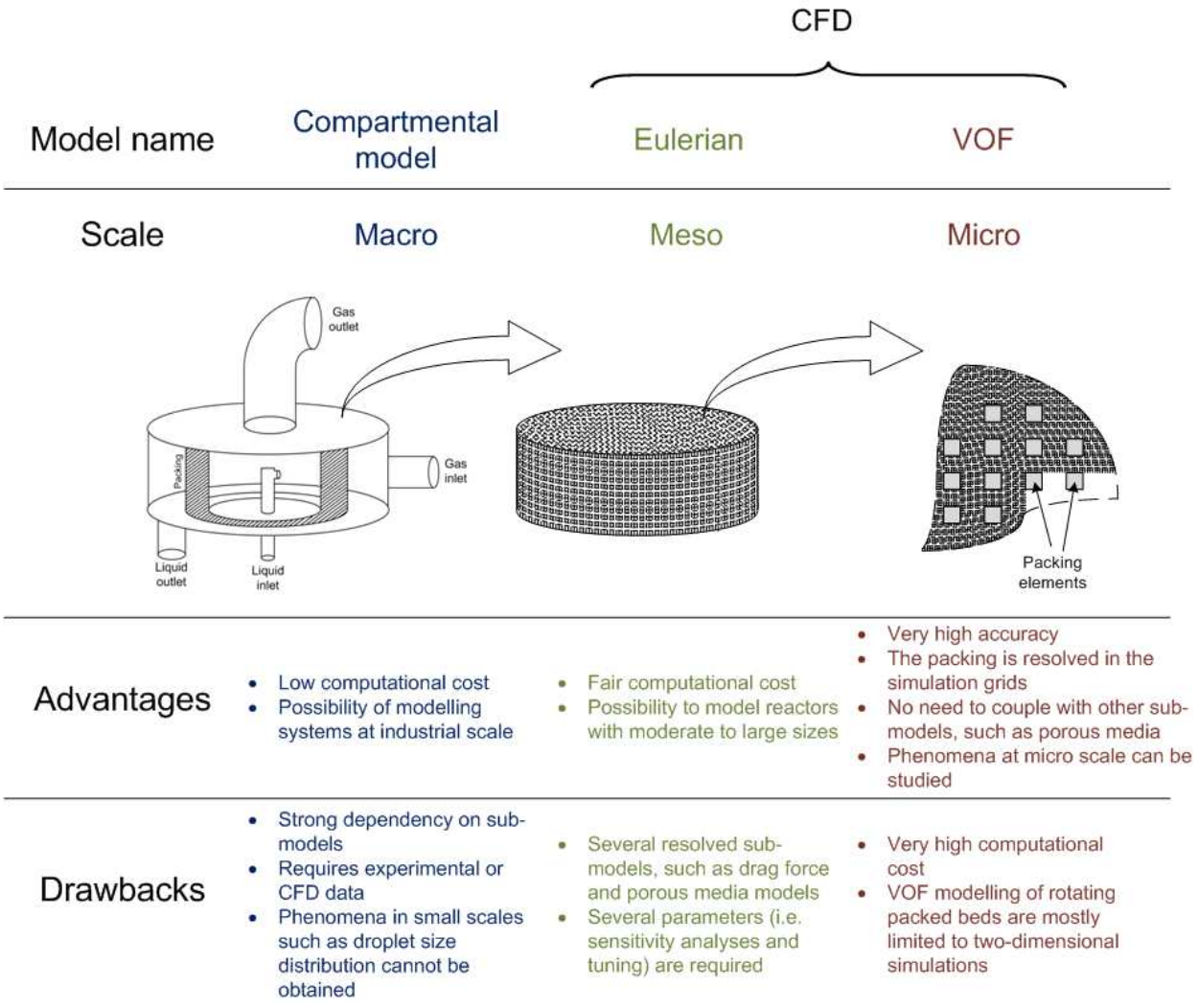

Figure 1. Details of different modeling approaches of RPBs, including modeling scale, limits advantages and disadvantages.

Due to their higher accuracy, CFD simulations can provide detailed insights into the micro-scaled phenomena [10, 22-28]. These phenomena include droplet-droplet and droplet-packing collisions, deformation of liquid jet and breakup into filaments and tiny droplets, and eventually the droplet size distribution. Droplet size distribution can be converted into mass transfer area in different sections of the RPB. Two main approaches have been mainly utilized in the CFD studies

of RPBs: micro-scale volume of fluid (VOF) and meso-scale Eulerian method. In the VOF method, the packing geometry is resolved in the simulation grids; consequently, the accuracy of the VOF simulation is potentially high. However, this small cell size leads to a large number of cells (≈1-50 million cells), which generates a high computational cost. Consequently, three-dimensional simulation of large RPBs using VOF are generally considered to be too computationally expensive [10]. Eulerian method aim to overcome this challenge. In Eulerian methods, the packing is not resolved in the simulation grids, but is taken into account through the addition of models for the porous packing, drag force and etc.. This approach enables researchers to model larger-scale RPBs, with the cost of increased model uncertainty and, generally, decreased accuracy [23, 24]. In the last few years, however, with the increase of computational resources, more researchers have become interested in using the VOF method for simulation of RPBs [22].

As the majority of the VOF simulations of RPBs were two-dimensional and utilized liquid holdup as the validation criterion and as the key element in the study of reactor hydrodynamics [10, 22, 25], two critical questions remain unanswered in the literature:

- Is liquid holdup a trustworthy criterion for mesh independency analysis, model validation and a key parameter in the study of the hydrodynamics of RPBs?
- Are the size and shape of droplets similar in two-dimensional and three-dimensional simulations? In other words, are the two-dimensional simulations adequate for studying the hydrodynamics of RPBs?

For the first question, mass transfer is known as the most significant parameter in studying the hydrodynamics of RPB, and mass transfer is primarily controlled by the interphase mass transfer area. Liquid holdup does not provide detailed information about the mass transfer area, while droplet size distribution can be directly converted into the interfacial mass transfer area.

Consequently, droplet size distribution should be studied as the key factor in studying RPB hydrodynamics instead of liquid holdup. However, investigation of droplet size distribution is more complex since droplets occur at the micro-scale, and VOF simulations with fine grids are required to capture the droplet dynamics accurately. For the second question, it is necessary to simulate a three-dimensional and compare the droplet size distribution to two-dimensional simulations. In this work, we address these two critical unanswered questions.

2. Models and methods

In this work, the VOF model was utilized to simulate the RPB. The simulations were performed using the interFoam solver of OpenFOAM® [32]. The governing equations of the model and the post-processing method to obtain the droplet size distribution are detailed in this section.

2.1. VOF model

In the VOF model, that was proposed initially by Hirt and Nichols [33], the equations of continuity and conservation of momentum are defined as:

$$\frac{\partial \rho}{\partial t} + \nabla.(\rho \vec{v}) = 0 \tag{1}$$

$$\frac{\partial (\rho \vec{v})}{\partial t} + \nabla.(\rho \vec{v}\vec{v}) = -\nabla p + \nabla.[\mu(\nabla \vec{v})] + \vec{F}_\sigma \tag{2}$$

where $\vec{F}_\sigma$ is the continuum surface force (surface tension force converted into a volumetric force) which can be modeled using [34]:

$$\vec{F}_\sigma = \sigma \frac{\rho k \nabla \alpha_l}{0.5(\rho_l + \rho_g)} \tag{3}$$

in which

$$k = \nabla.\left(\frac{\nabla.\alpha_i}{|\nabla.\alpha_i|}\right) \tag{4}$$

where α shows volume fraction and i stands for the phases (liquid and gas) present in the reactor and ρ, μ are volume-averaged density and viscosity of grid cells which can be defined as:

$$\rho = \alpha_l \rho_l + \alpha_g \rho_g \tag{5}$$

$$\mu = \alpha_l \mu_l + \alpha_g \mu_g \tag{6}$$

in which

$$\alpha_l + \alpha_g = 1 \tag{7}$$

The interface between the two phases is tracked using the following equation:

$$\frac{\partial(\alpha_i \rho_i)}{\partial t} + \nabla.(\alpha_i \rho_i \vec{v}_i) = 0 \tag{8}$$

Although it is reported that a small part of the liquid film flow near the packing elements may develop into turbulent flow [35], based on our calculations, the maximum liquid phase Reynolds number on packing elements:

$$\mathrm{Re}_l = \frac{\rho_l u_\infty d_e}{\mu_l} \tag{9}$$

was approximately 1612. This value shows a laminar/transient regime in the studied RPBs. To further investigate the flow regime, we compared the laminar and turbulent (*k*-epsilon model) simulation of a single case. In other words, we assessed the accuracy of laminar flow assumption by carrying out an unsteady Reynolds-averaged Navier-Stokes (URANS) simulation and comparing the results.

For the rotation of packing in the RPB, a sliding mesh model using the Arbitrary Mesh Interface (AMI) of OpenFOAM was utilized. AMI enables the simulations of disconnected adjacent mesh domains. This is achieved by coupling disconnected regions and ensuring that the fluxes are conserved at their interfaces by a correct distribution of the fluxes. This is useful to simulate rotating geometries like RPBs. To this end, we require separate meshes for the static and rotating regions of the RPB. These regions are coupled at patch boundaries using *cyclicAMI* boundary condition. Details of the arbitrary mesh interface (AMI) are out of this article's scope and can be found in [36].

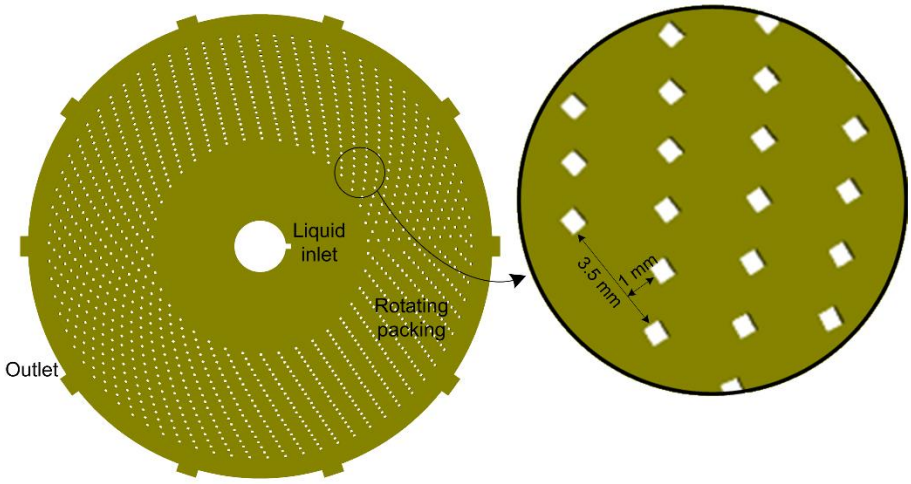

Figure 2. Schematics of the rotating packed bed.

2.2. RPB geometry and operating conditions

Figure 2 shows the geometry of the simulated RPB. This geometry was selected based on previous experimental research [20] and CFD simulations [10]. Dimensions of the simulated RPB are reported in Table 2. Similar to the previous VOF simulations [10], uniform inlet velocity, no-slip, moving wall, and ambient pressure boundary conditions were considered at the liquid inlet,

walls, packing elements, and outlet, respectively. It should be mentioned that for the model validation, ten outlets were considered at the outer periphery, similar to previous research [10]. We observed that by using this method, the liquid holdup inside the reactor would become a strong function of the size ratio of the outlet to wall at the outer periphery. As a result, in the main simulations (all the simulations except validation), we considered the entire outer periphery as an outlet. This is explained in detail in the following sections of this article. For the three-dimensional simulations, five and ten layers of the same mesh used in two-dimensional were considered, and symmetry boundary condition was utilized in the axial direction.

Table 2. Dimensions of the simulated RPB.

Parameter	**Value**
Bed outer diameter	9 cm
Bed inner diameter	1 cm
Liquid inlet length	1 mm
Packing element length	0.5 mm
Lateral distance between packing elements	3.5 mm
Radial distance between packing elements	1 mm

The geometry of the RPB was designed according to previous research of Xie et al. [10] and experiments of Yang et al. [20]. The packing consists of 21 concentric layers, where the circumferential and radial distance between packing wire elements are 3.5 and 1 mm, respectively, and the length of each wire mesh is 0.5 mm. Using this packing arrangement, the specific area and

void fraction of the packing are 469 m^{-1} and 0.94, respectively [10]. Other details about the geometry of the RPB can be found in [10, 20].

In Tables 3 and 4, the simulations' operating conditions and the physical properties of the simulation material are reported. All the operating condition values and ranges were taken from our validation source [10, 20]. The superficial velocity of the liquid at the inlet, u_l, is calculated using:

$$u_l = \frac{Q_l}{A_i} \tag{10}$$

2.3. Image processing

Image processing was utilized to obtain the liquid holdup and droplet size distribution in the simulated RPB. Image processing was performed using a code written in Matlab. At the beginning of each rotation (after reaching steady-state operation), a screenshot from the simulation was captured. All the screenshots were converted into binary images, and finally, the droplet size distribution was obtained. For converting the calculated number of pixels inside the droplets to the droplet area, the number of pixels inside an object with a specified area was calculated, and the conversion coefficient was found.

3. Results and discussion

3.1. Image processing calibration

Before using the image processing to obtain droplet size distribution, a sensitivity analysis on the number of pixels in the captured images is required. For this purpose, for a single time-step from simulation 20, in Table 3, three images with three different numbers of pixels (1508×1508,

3016×3016, and 6032×6032) were taken. For each image, the calibration was performed with an object of a pre-specified area with the same number of pixels as the image. Figure 3 shows the droplet size distribution and number of droplets obtained from these three images. As can be observed from this figure, the droplet size distributions and the number of droplets from these three resolutions do not highlight any significant difference. As a result, the image resolution of 1508×1508 was used for image analysis in this research.

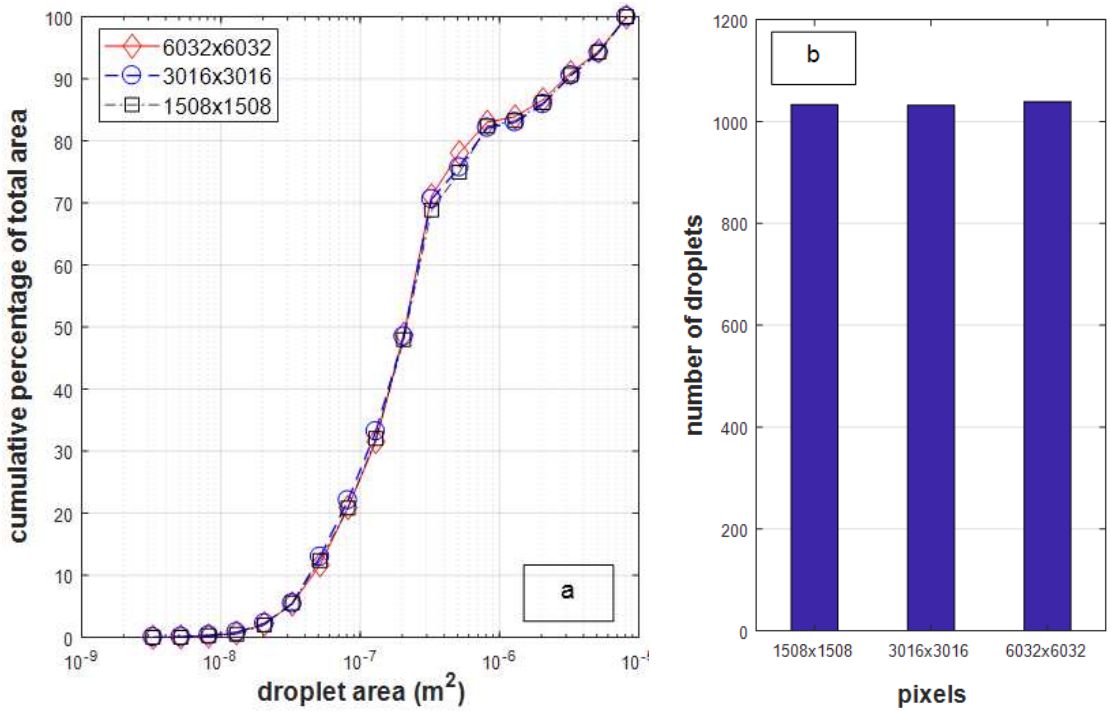

Figure 3. Effect of image resolution on a) droplet size distribution and b) number of droplets.

Table 3. Operating and geometrical properties of the simulations in this work.

Case no.	u_l (m/s)	ω (rpm)	$L_{grid,max}$ (μm)	Dimension	Outlet BC.	Model
1	1.5	500	150	2D	Outlet	laminar
2	1.5	500	100	2D	Outlet	laminar
3	1.5	500	50	2D	Outlet	laminar

4	1.5	500	100	3D-5	Outlet	laminar
5	1.5	500	100	3D-10	Outlet	laminar
6	1.5	500	100	2D	Outlet-Wall	laminar
7	1.5	250	100	2D	Outlet	laminar
8	1.5	1500	100	2D	Outlet	laminar
9	1.5	1500	75	2D	Outlet	laminar
10	1.5	1500	50	2D	Outlet	laminar
11	1.5	1500	50	2D	Outlet-Wall	laminar
12	1.5	1500	42	2D	Outlet	laminar
13	1.5	1000	50	2D	Outlet	laminar
14	1.5	1000	50	2D	Outlet-Wall	laminar
15	2.87	500	100	2D	Outlet	laminar
16	2.87	500	50	2D	Outlet	laminar
17	2.87	250	100	2D	Outlet	laminar
18	2.87	1500	100	2D	Outlet	laminar
19	2.87	1500	50	2D	Outlet	laminar
20	2.87	1500	42	2D	Outlet	laminar
21	2.87	1000	50	2D	Outlet	laminar
22	1.5	1500	50	2D	Outlet	k-epsilon
23	2.0	250	100	2D	Outlet	laminar
24	2.0	500	100	2D	Outlet	laminar
25	2.0	1000	50	2D	Outlet	laminar
26	2.0	1500	50	2D	Outlet	laminar
27	2.87	1500	50	2D	Outlet-Wall	laminar
28	2.0	1500	50	2D	Outlet-Wall	laminar

Table 4. Physical properties of the simulation materials.

Parameter	Value
ρ_g	1.3 (kg/m^3)
ρ_l	1000 (kg/m^3)
μ_g	1.8×10^{-5} kg/(m·s)
μ_l	0.0012 kg/(m·s)

σ	0.07 (N/m)

It should be mentioned that for the calculation of the droplet area, we assumed that the droplet is circular, and its effective diameter was calculated using the following equation:

$$d_d = \sqrt{\frac{4A_d}{\pi}} \tag{11}$$

3.2. Model validation

As mentioned earlier, in previous CFD simulations of RPBs, the liquid holdup was generally used as the mesh dependency analysis and the key parameter to study these beds' hydrodynamics. This may have several drawbacks, including:

- Liquid holdup strongly depends on the definition of specified boundary conditions at the outer periphery of two-dimensional simulations
- It does not provide any detailed information about the droplet size distribution, which is the information that can be converted into an active interphase mass transfer area.

We should note that droplet size distribution is a phenomenon occurring at one scale smaller than liquid holdup. By reaching grid independence on droplet size distribution, this independence applies to the liquid holdup as well. As a result, we used droplet size distribution for the mesh dependency analysis and the key parameter in studying the hydrodynamics of RPBs. However, for the model validation, the liquid holdup was utilized since it was the only available information in previous research [10].

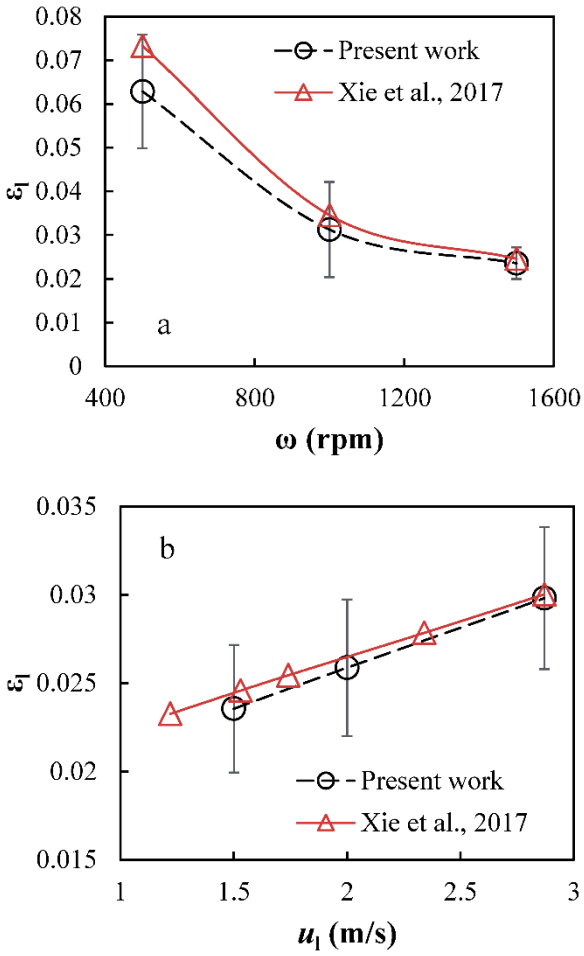

Figure 4. Comparison of liquid holdups of a: cases 6, 11, 14 and b: cases 11, 27 and 28 and previous work of Xie et al. [10] (confidence level = 95% for error bars).

Figure 4 shows the comparison of calculated liquid holdup in cases 6, 11, 14, 27 and 28 with previous research [10] on the same RPB design and operating conditions. It should be mentioned that to keep the boundary and operating conditions similar to the reference work [10], ten outlets with the same size defined by Xie et al. [10] were considered on the outer periphery, while the rest of the outer periphery was defined as a wall. Figure 4 shows that our VOF simulation results are in good agreement with Xie et al [10], and the model can be used to investigate the hydrodynamics of RPBs further. We noticed that liquid holdup's value is a function of the ratio of outlet to wall at

the outer periphery during our simulations. Furthermore, considering a combination of wall and outlet at the outer periphery is unrealistic in two-dimensional simulations since the liquid outlet in a real RPB is located at the bottom of a cylindrical bed in the axial direction. As a result, it is decided to define the entire outer periphery as an outlet for the rest of our research simulations.

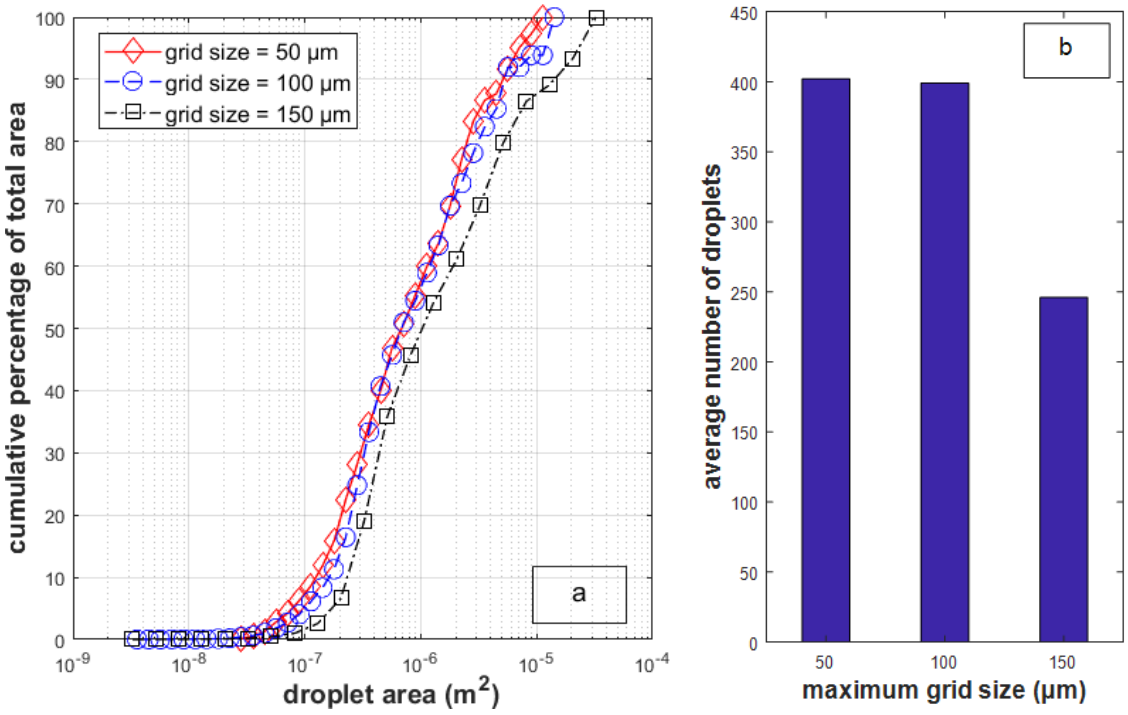

Figure 5. Grid dependency analysis for cases with u_l = 1.5 m/s and ω = 500 rpm (cases 1-3 in Table 3).

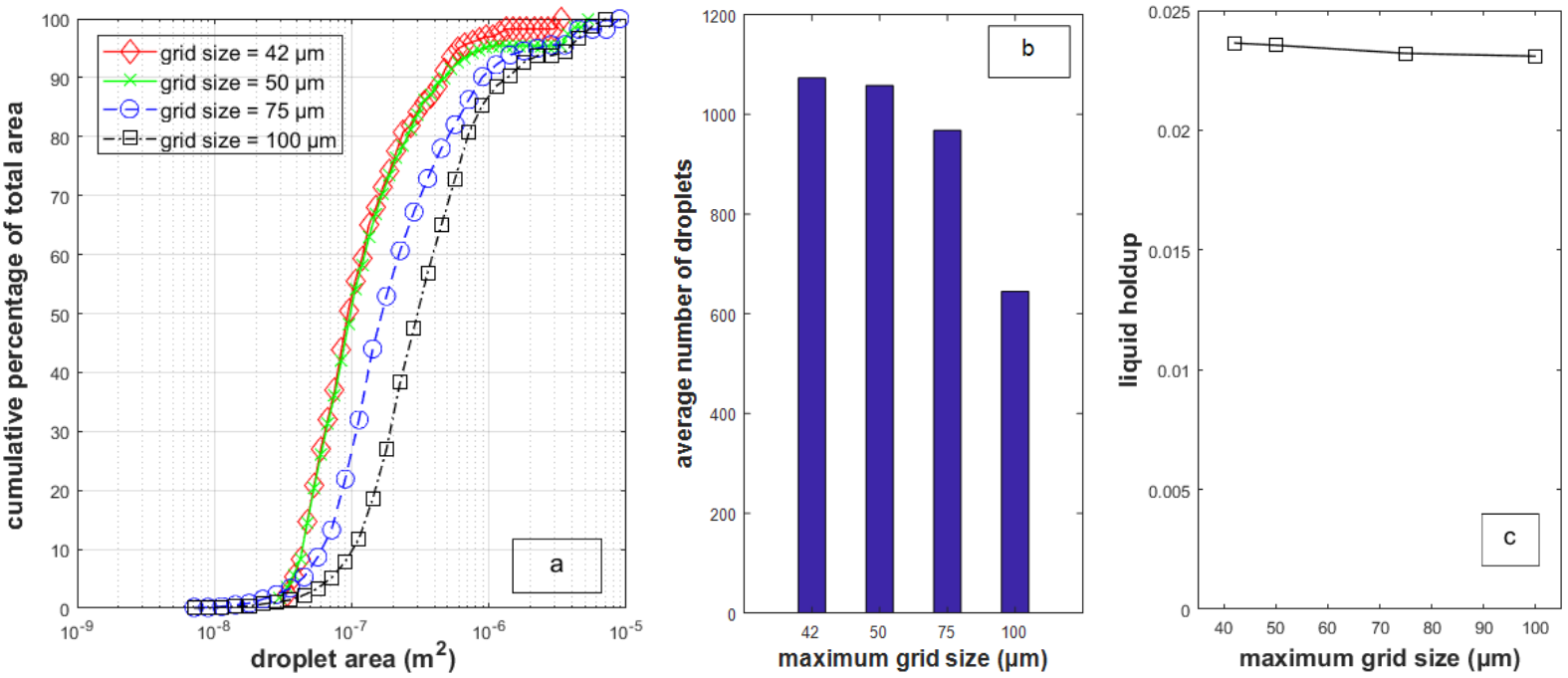

Figure 6. Grid dependency analysis for cases with u_l = 1.5 m/s and ω = 1500 rpm (cases 8, 9, 10 and 12 in Table 3).

3.3. Grid dependency analysis

As mentioned earlier, droplet size distribution is used for grid dependency analysis in this research. RPB geometries were created with five characteristic cell sizes of 150, 100, 75, 50, and 42 μm. Figure 5 shows the grid dependency analysis results for the case with u_l = 1.5 m/s and ω = 500 rpm (cases 1-3 in Table 3). From this figure, it is observed that decreasing the grid size from 100 μm to 50 μm, the number of droplets and the droplet size distribution do not change significantly. Consequently, the geometry with the maximum grid size of 100 μm was used for u_l = 1.5 m/s, ω = 500 and 250 rpm. The same analysis was performed for u_l = 1.5 m/s and ω = 1500 rpm (cases 8, 9, 10 and 12), u_l = 2.87 m/s and ω = 500 rpm (cases 15 and 16), and u_l = 2.87 m/s and ω = 1500 rpm (cases 18-20) using geometries with different mesh sizes. Figures 6, 7, and 8

show the results of these analyses, respectively. From Figures 6-8, the maximum grid size of 50 μm for cases with u_l = 1.5 m/s, ω = 1500 and 1000 rpm; maximum grid size of 100 μm for cases with u_l = 2.87 m/s, ω = 500 and 250 rpm; and maximum grid size of 50 μm for the case with u_l = 2.87 m/s and ω = 1000 were selected. For a single case (in Figure 6), we compared the liquid holdups obtained from simulations with different cell sizes (Figure 6c). It was observed that using liquid holdup, grid independence is achieved at large cell size. Indeed, from the coarsest grid (100 μm) to the finest grid (42μm) the liquid holdup varied by less than 2.5%, whereas the droplet size distributed was altered drastically. This proves that droplet size distribution is a more reliable criterion to be used for grid dependency and for investigation of the hydrodynamics of RPBs. It is to be noted that the liquid hold-up was used by multiple authors [10, 22] to assess grid independence. The hold-up should not be used as a criterion fashion if the simulation aims at predicting the full hydrodynamics, the droplet size distribution or the mass transfer area since those quantities are much-more mesh dependent.

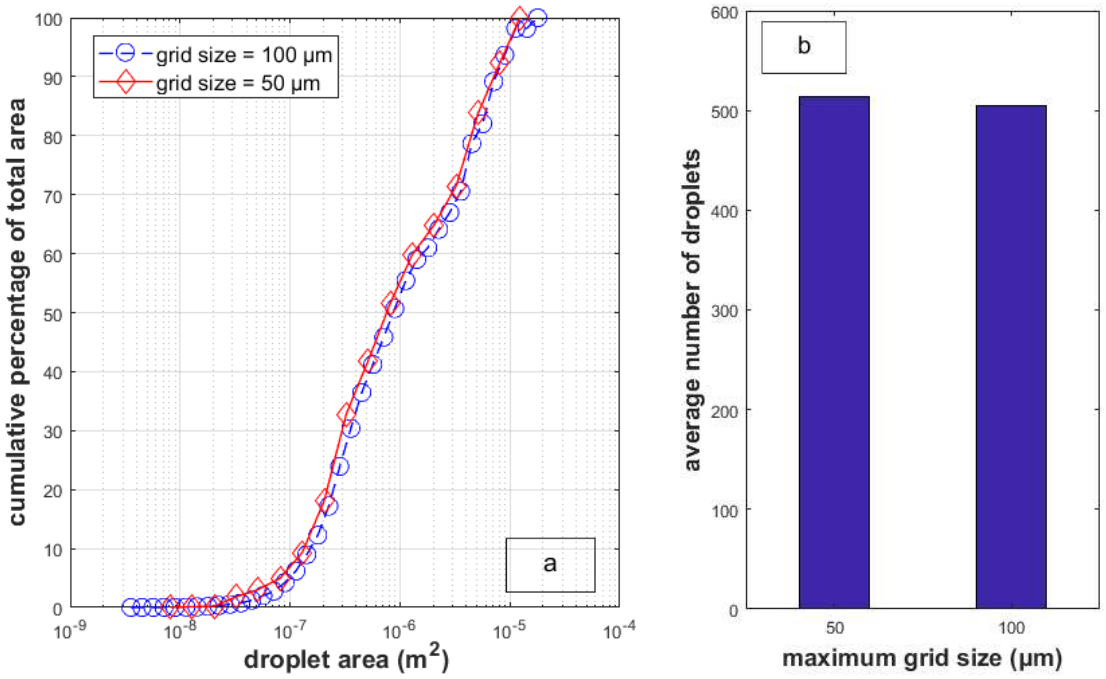

Figure 7. Grid dependency analysis for cases with u_l = 2.87 m/s and ω = 500 rpm (cases 15 and 16 in Table 3).

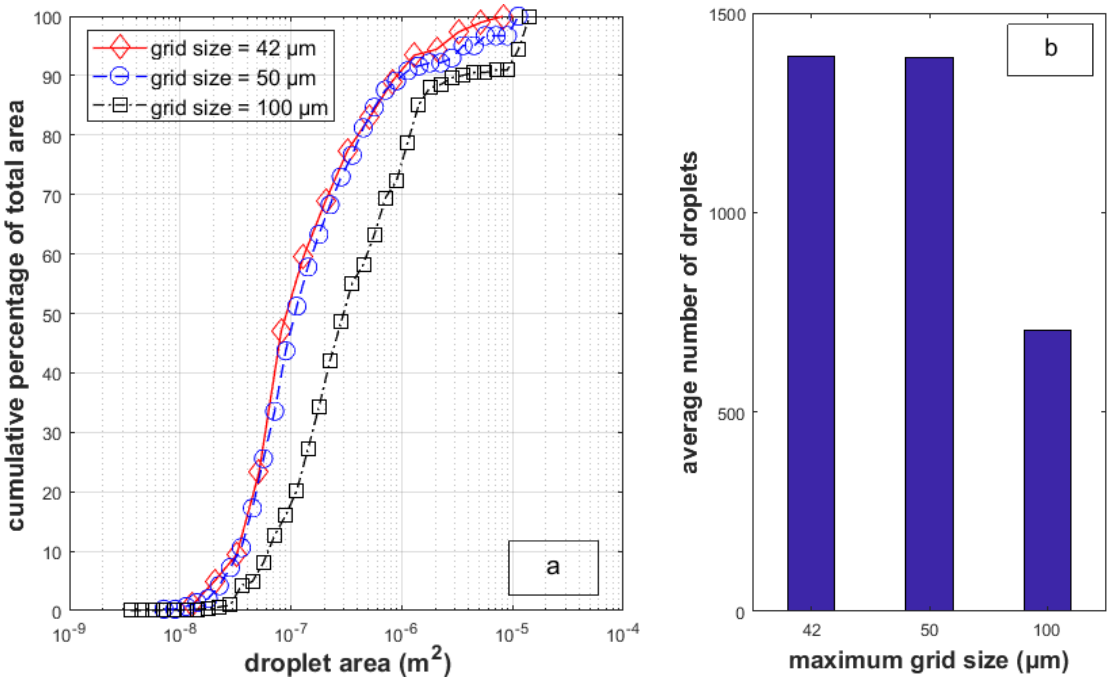

Figure 8. Grid dependency analysis for cases with u_l = 2.87 m/s and ω = 1500 rpm (cases 18-20 in Table 3).

3.4. Two-dimensional vs. three-dimensional simulations

One of the critical unanswered questions in the VOF simulations of RPBs is whether two-dimensional simulations illustrate the hydrodynamics of RPBs accurately. Formation, breaking, coalescence, droplet-droplet, and droplet-packing collisions are a few examples of significant three-dimensional phenomena. As a result, to study the hydrodynamics of RPBs using two-

dimensional simulations, we have to make sure that two-dimensional simulations are adequately accurate.

For this purpose, a sample two-dimensional case (case 2) was chosen and five and ten layers of the grid were added (cases 4 and 5, respectively) in the axial direction to provide a three-dimensional grid. The droplet size distributions obtained from two-dimensional and three-dimensional simulations were compared. The post-processing code converts the area of droplets into droplet diameter in two-dimensional simulations, while in three-dimensional simulations the volume of spherical droplets are converted into droplet diameter. Figure 9 shows the results of this comparison. It can be observed that the droplet size distribution from two-dimensional simulations does not have a significant difference compared to three-dimensional simulations. Consequently, two-dimensional simulations of RPBs are trustworthy in order to study the droplet size distribution and hydrodynamics of RPBs.

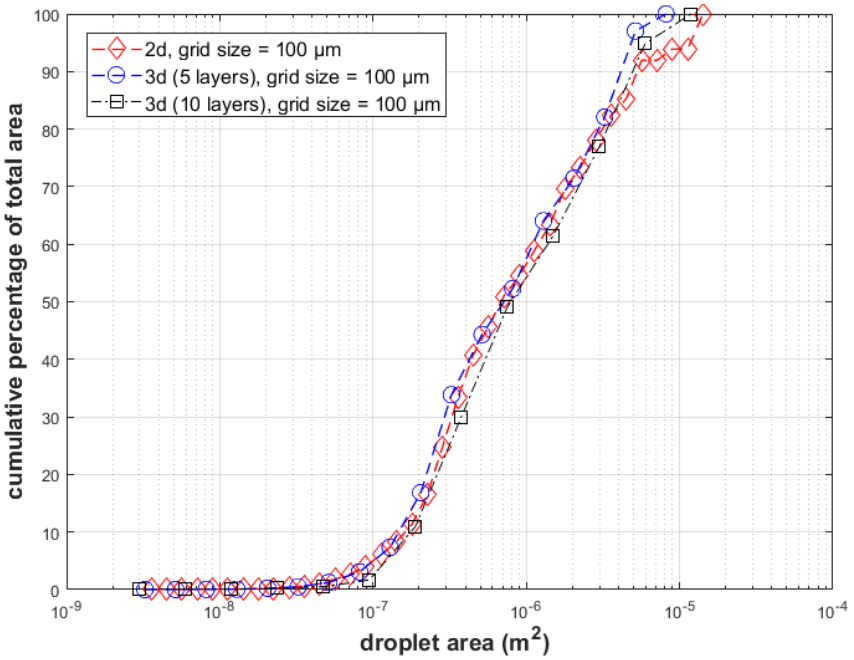

Figure 9. Comparison of droplet size distribution obtained from two-dimensional and three-dimensional simulations (cases 2, 4 and 5).

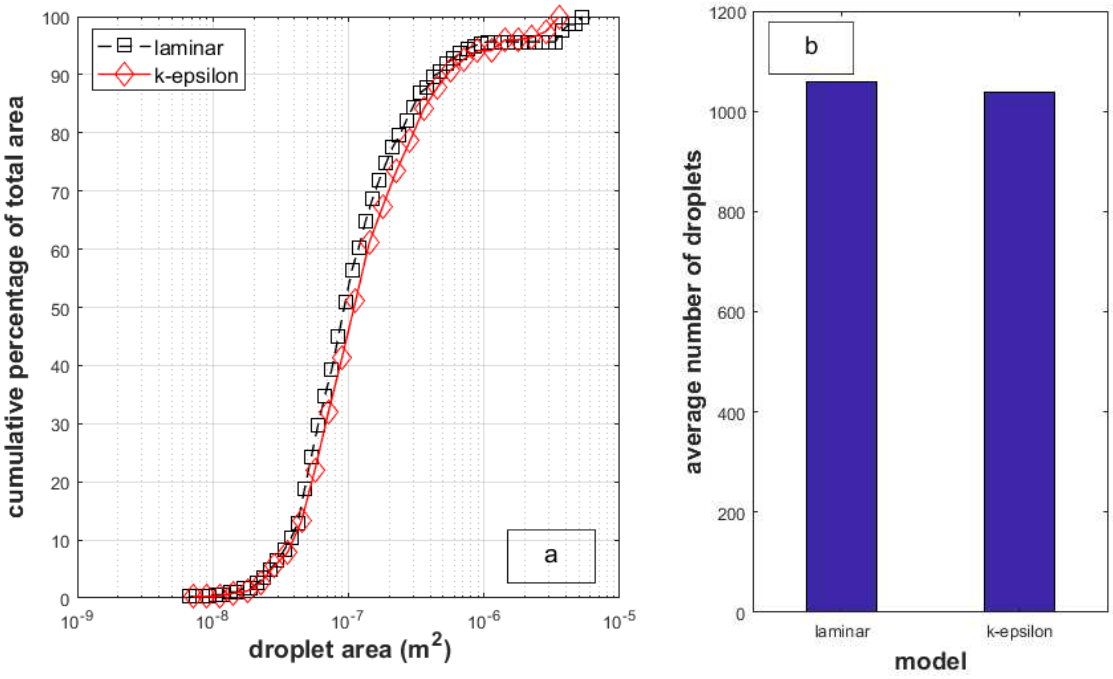

Figure 10. Comparison of laminar and turbulence models for cases 10 and 22 (u_l = 1.5 m/s, ω = 1500 and $L_{grid,max}$ = 50 μm).

3.5. Flow regime

As discussed previously, according to the value of the maximum Reynolds number, the flow regime inside the studied RPB should be laminar. To further investigate this assumption, a comparison is performed between results of a single case (cases 10 and 22, in which u_l = 1.5 m/s, ω = 1500 and $L_{grid,max}$ = 50 μm) simulated with laminar and turbulent flow regimes. It should be mentioned that the *k*-epsilon model was utilized to model turbulence. Figure 10 shows the results of this comparison. It can be observed that the droplet size distributions and the average number of droplets obtained from laminar and turbulent simulations are very close. In other words, it can

be concluded that the majority of possible turbulent structures in the RPB were captured by the fine mesh used in this study. As a result, we used the laminar flow assumption for the simulation of the RPB in this research.

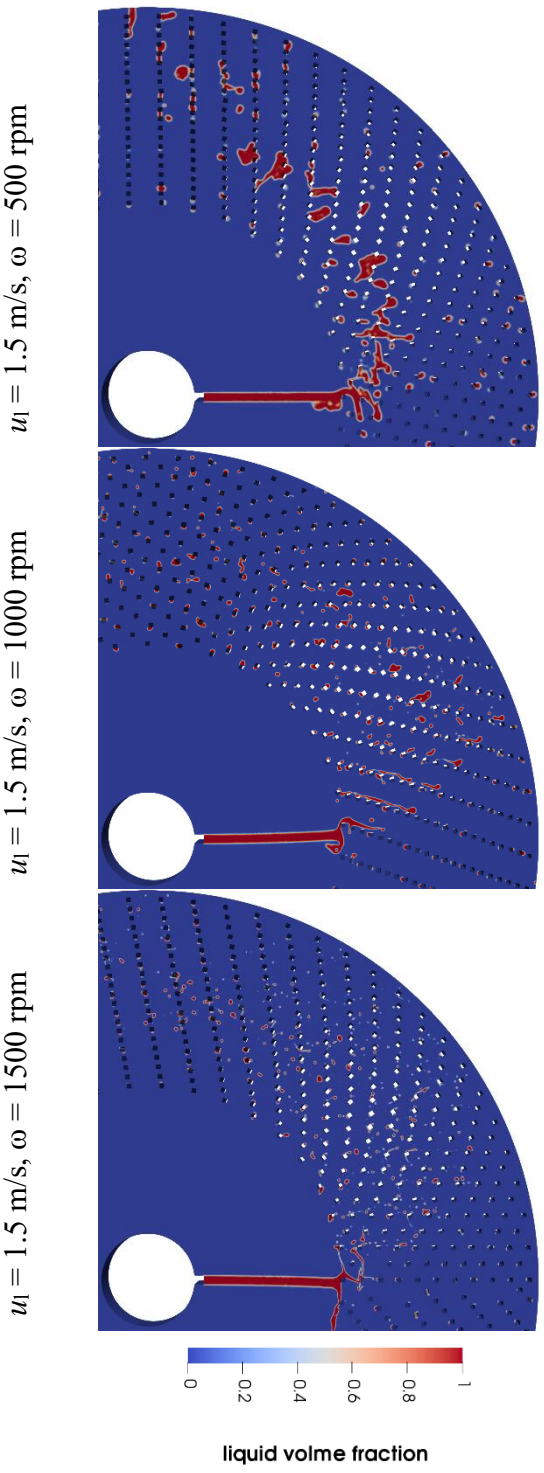

Figure 11. Screenshots from simulations (u_l = 1.5 m/s, ω = 500, 1000 and 1500 rpm) during steady-state operation.

3.6. Flow pattern in RPB

Figure 11 shows screenshots of the simulations (u_l = 1.5 m/s, ω = 500, 1000 and 1500 rpm) during steady-state operation of RPB. The decrease in the droplet size distribution with increasing rotational speed is evident. As can be observed, the liquid jet hits the rotating packing elements, and it is broken into tiny filaments and droplets in the packing region. It can also be observed that a small part of the inserted liquid deposits on the packing elements and rotates with the packing. This phenomenon was also observed and reported in previous research [10]. With increasing rotational speed, the ratio of deposited liquid on the packing to total inserted liquid decreases (which results in smaller liquid holdup [10, 20]). Mundo et al. [43] studied the hydrodynamics of droplet-wall collisions and found a critical Ohnesorge number (Oh), below which the droplet deposits on the wall during a droplet-wall collision. The Ohnesorge number and its critical value are defined as:

$$Oh_{d-w} = \frac{\mu_l}{\sqrt{\rho_l \sigma d_d}} \tag{12}$$

$$Oh_{cr} = 57.7\,\mathrm{Re}_{d-w}^{-1.25} \tag{13}$$

where d_d and σ are droplet size and surface tension, and Re is defined based on the relative velocity of droplet and wall [43]. In the literature [6], it is reported that the velocity of droplets in the packing region is very close to the linear velocity (r.ω) of the rotating packing. Therefore, the value of $\mathrm{Re}_{d\text{-}w}$ is relatively small in RPBs. This leads to a relatively large critical Ohnesorge number ($\mathrm{Oh}_{cr} \approx 0.1$), while the Ohnesorge number in the simulated RPBs is in the range of 0.02 – 0.06

(≈0.02 for cases with ω = 250 rpm and ≈0.06 for cases with ω = 1500 rpm). As a result, a portion of the injected liquid always deposits on the packing elements, while its ratio decreases with increasing the rotational speed. In other words, a smaller portion of the total inserted liquid deposits on the packing and surface renewal becomes more favorable at higher rotational speeds.

As mentioned earlier, in this research, we focused on the droplet size distribution as the key parameter in studying the hydrodynamics of RPBs. Figure 12 shows the radial distribution of average droplet size in the packing region and the corresponding Weber numbers (We) at various liquid inlet velocities and rotating speeds. It has been previously reported that the hydrodynamics of RPBs is complex, and several simultaneous physical and chemical phenomena affect the hydrodynamics [10, 20]. Figure 12 illustrates this complexity as the droplet diameter's radial distributions vary with changing the rotational speed with no constant trend.

As a simplified model, we assumed that the droplet-packing collision (which leads to the breakup of droplets) and droplet-droplet coalescence govern the droplet size distribution. Several studies were conducted on the investigation of secondary droplet shape and size after a breakup [37, 38]. It is reported that the droplet breakup regime (i.e., post-breakup size) is determined mainly by the We number, which can be defined as [39]:

$$We = \frac{\rho_l d_d V_r^2}{\sigma} \tag{14}$$

where V_r is the relative velocity, which can be defined as [39]:

$$V_r = \sqrt{V_d^2 + V_p^2 - 2V_d V_p \cos\gamma} \tag{15}$$

in which V_d, V_p, and α are the velocity of the droplets, the linear velocity of packing at the collision point (r.ω), and the impact angle, respectively. Based on We's value, the collisions can be divided

into several regimes, which are illustrated in Figure 13. These regimes include no breakup (We<3), vibrational (3<We<10), bag (10<We<35), bag-stamen (35<We<80), shear (80<We<350), and catastrophic breakup (We>350). These mechanisms are divided in Figure 12 using blue dashed lines.

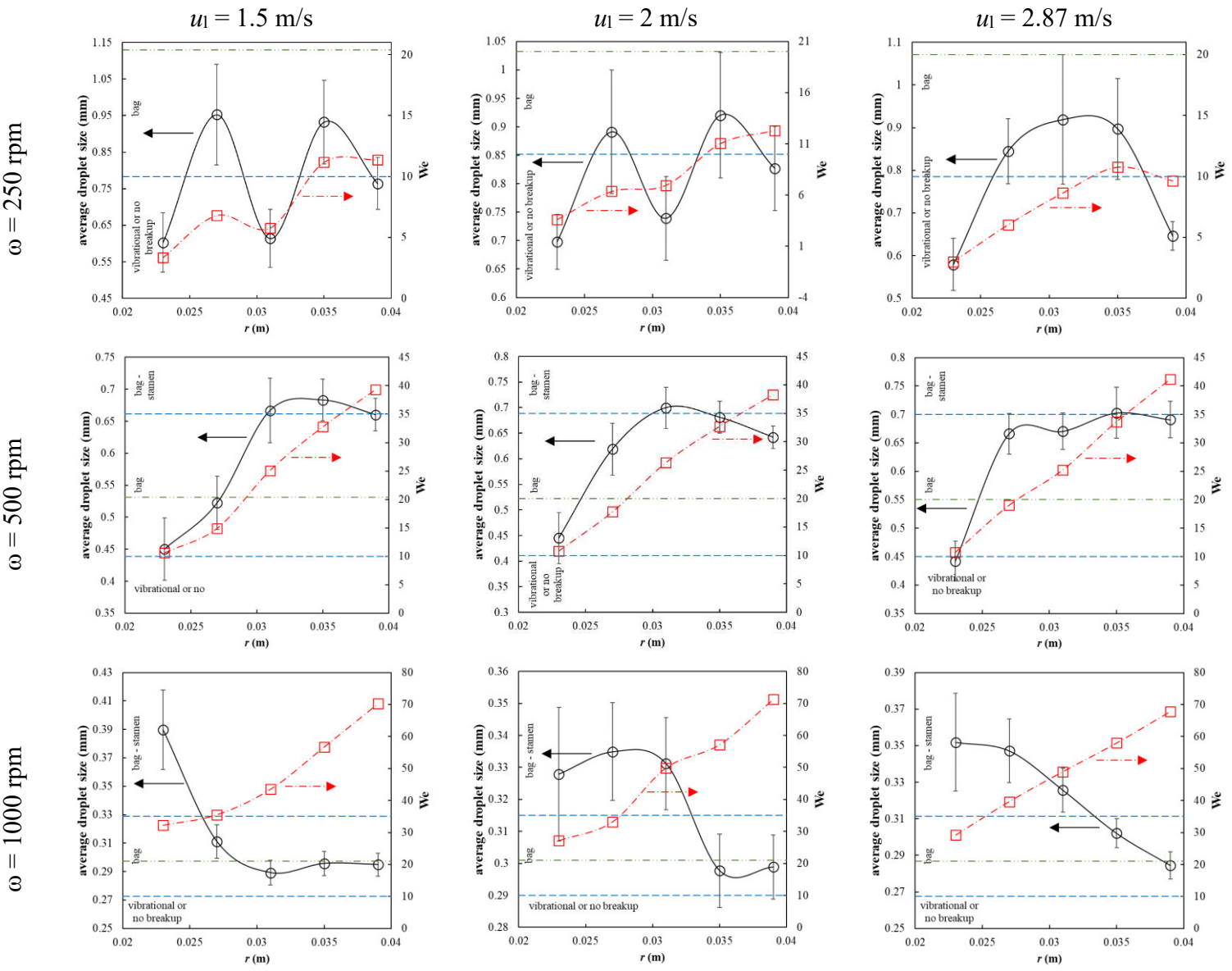

ω = 1500 rpm

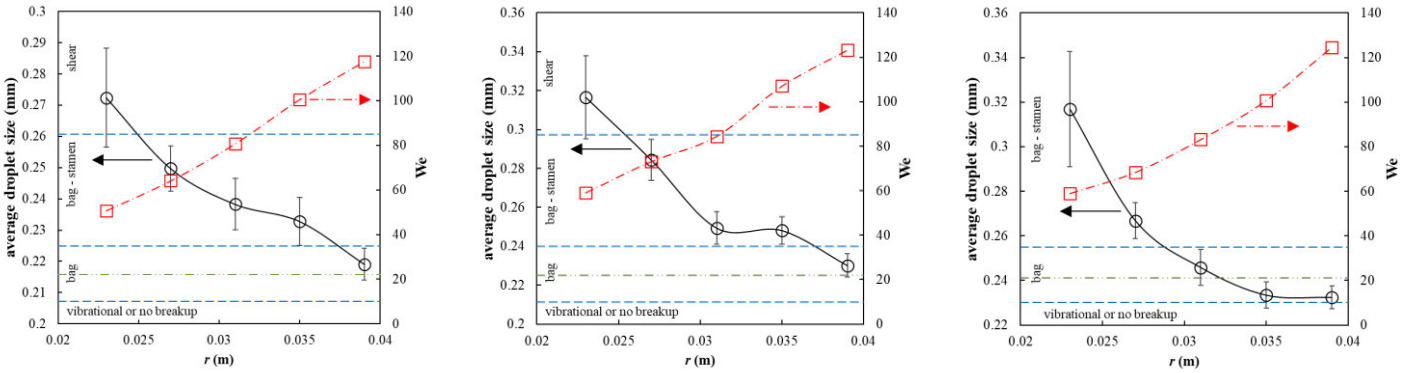

Figure 12. Radial distribution of average droplet size in the packing and the corresponding Weber numbers at various liquid inlet velocities and rotating speeds. Red and black lines on these figures show Weber number and average droplet size, respectively.

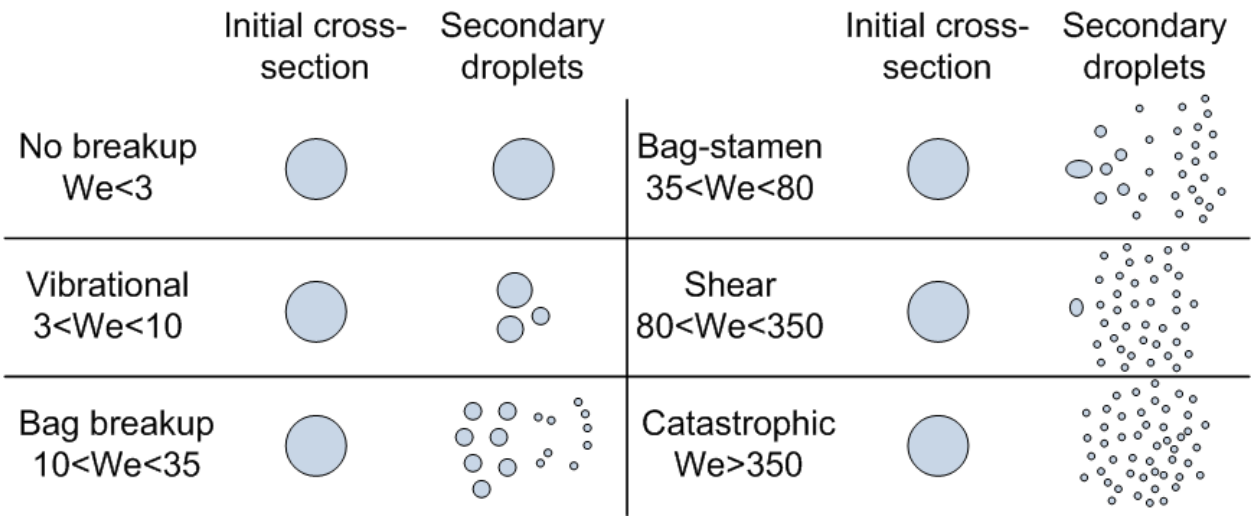

Figure 13. Different breakup mechanisms of droplets based on Weber number [37, 40].

Similarly, a two-parameter model is proposed to estimate droplet coalescence during droplet-droplet collisions in liquid sprays [41]. In this model, at each impact parameter, *b*, a range of We number is specified. In this specified range, the coalescence mechanism is dominant

compared to other mechanisms, such as bouncing and stretching. Impact parameter can be defined as:

$$b = \frac{2B}{d_1 + d_2} \tag{16}$$

where d_1 and d_2 are droplet diameters before the collision and B is the distance between the centers of the droplets in a plane perpendicular to the relative velocity vector [41]. In other words, the impact parameter, b, is a dimentionaliess expression of the distance B. Definition of B and other details of implementing this model can be found elsewhere [42]. The threshold value of We, below which droplet coalescence is dominant, is illustrated using green dashed lines in Figure 12.

Based on the breakup and coalescence models of droplets, the trends observed in Figure 12 can be explained. From Figure 12, it can be observed that rotational speed significantly affects the radial distribution of the average droplet diameter. At the same time, the effect of liquid inlet velocity is not significant. At ω = 250 rpm, the radial distribution of the average droplet size shows a fluctuating trend. At smaller radii, the dominant breakup regimes are not breakup and vibrational, while all the Weber numbers are located in the coalescence-dominant regime. At the largest radius, the breakup mechanism changes to the bag regime, which leads to a lower average droplet diameter.

At ω = 500 rpm, the radial distribution of the average droplet diameter shows increasing-constant trends. At the first two smaller radii, the breakup mechanism is bag, and the points are in the coalescence zone. As a result, the average droplet size increases. At the next two radii, the breakup regime is still bag, while the points are not located in the coalescence zone anymore. Therefore, the breakup and coalescence nullify each other, and the droplet size stays approximately

constant. The breakup regime changes to bag-stamen at the largest radius and the average droplet size slightly decreases.

At higher rotational speeds (ω = 1000 and 1500 rpm), all the points are in the no-coalescence zone, while the breakup regimes are bag and bag-stamen regimes at ω = 1000 rpm, and bag-stamen and shear regimes at ω = 1500 rpm. Consequently, the average droplet size generally decreases at the mentioned rotational speeds. To conclude, it can be claimed that in order to obtain smaller diameter sizes (i.e. larger mass transfer area), the *We* number should be in the shear breakup regime and the RPB should be designed to operate in the no-coalescence limit.

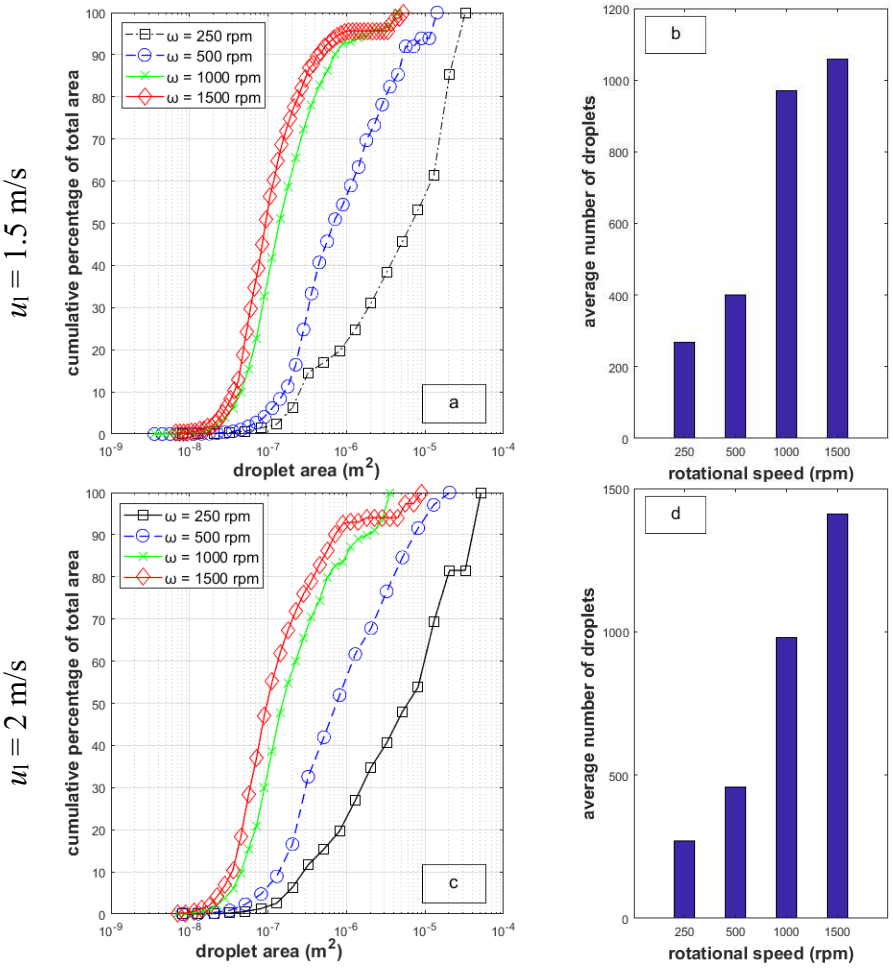

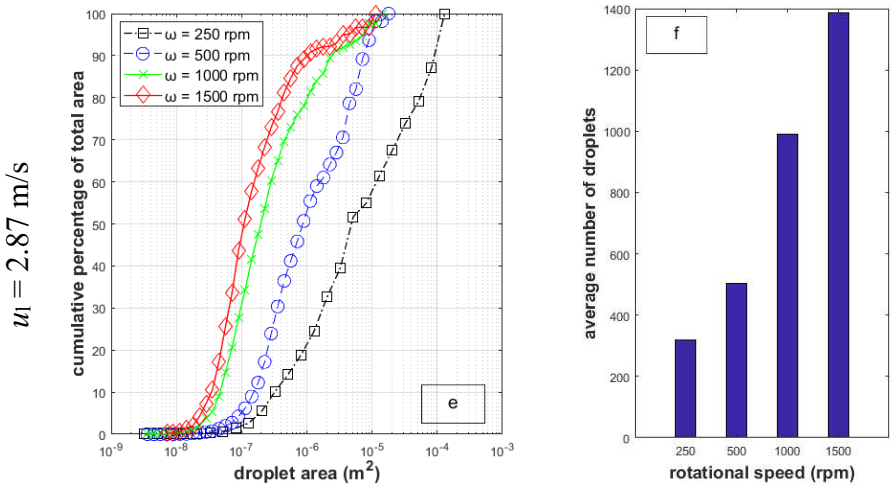

Figure 14. Effect of rotational speed on the droplet size distribution and average number of droplets at a, b) u_l = 1.5 m/s, c, d) u_l = 2 m/s and e, f) u_l = 2.87 m/s.

3.7. Effect of rotational speed

This section investigates the effect of rotational speed on the droplet size distribution and the average droplet size. Figure 14 shows the effect of rotational speed on the droplet size distribution at three different liquid inlet velocities (u_l = 1.5, 2, and 2,87 m/s). Increasing the rotational speed at all three liquid inlet velocities leads to smaller droplet sizes. However, as the rotational speed increases further, this effect diminishes. In other words, there is a limit for the rotational speed, beyond which, with further increasing the rotational speed, the droplet size distribution remains constant. We hypothesize that this limit could be overcome by increasing the We larger than 350 to change the breakup mechanism to catastrophic.

The number of droplets also increases with increasing the rotational speed. With increasing the rotational speed from 500 rpm to 1000 rpm, a significant jump can be observed at all the inlet liquid velocities, which can be attributed to the operation of the RPB at bag-stamen and shear breakup regimes and no-coalescence at these rotational speeds. Figure 15 shows the effect of

rotational speed on the average droplet size. It can be observed that the average droplet sizes at different liquid inlet velocities are approximately equal. The same decreasing trend of average droplet size with rotational speed was reported in previous research [6, 28]. The standard deviation of the droplet size also decreased with increasing rotational speed. In other words, the droplets have more uniform sizes with increasing rotational speed.

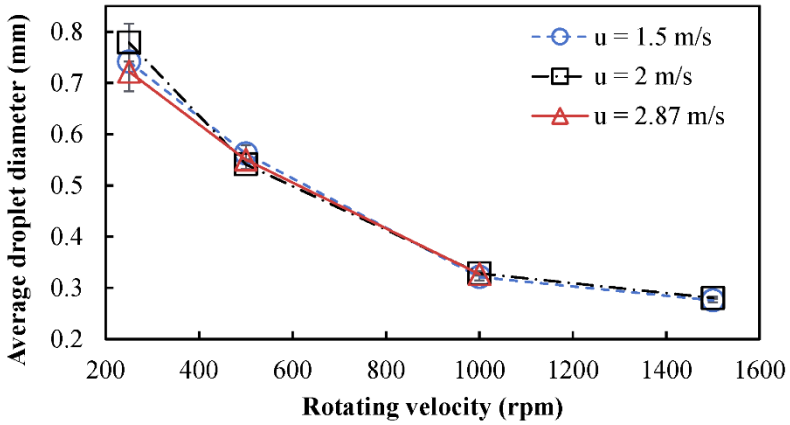

Figure 15. Effect of rotational speed on the average droplet size.

ω = 250 rpm

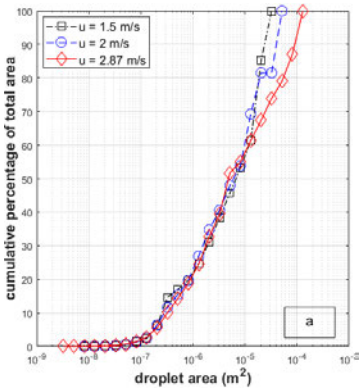

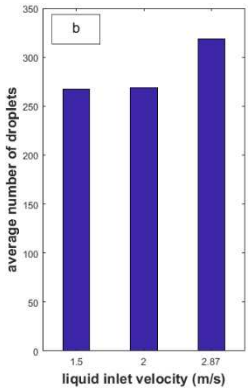

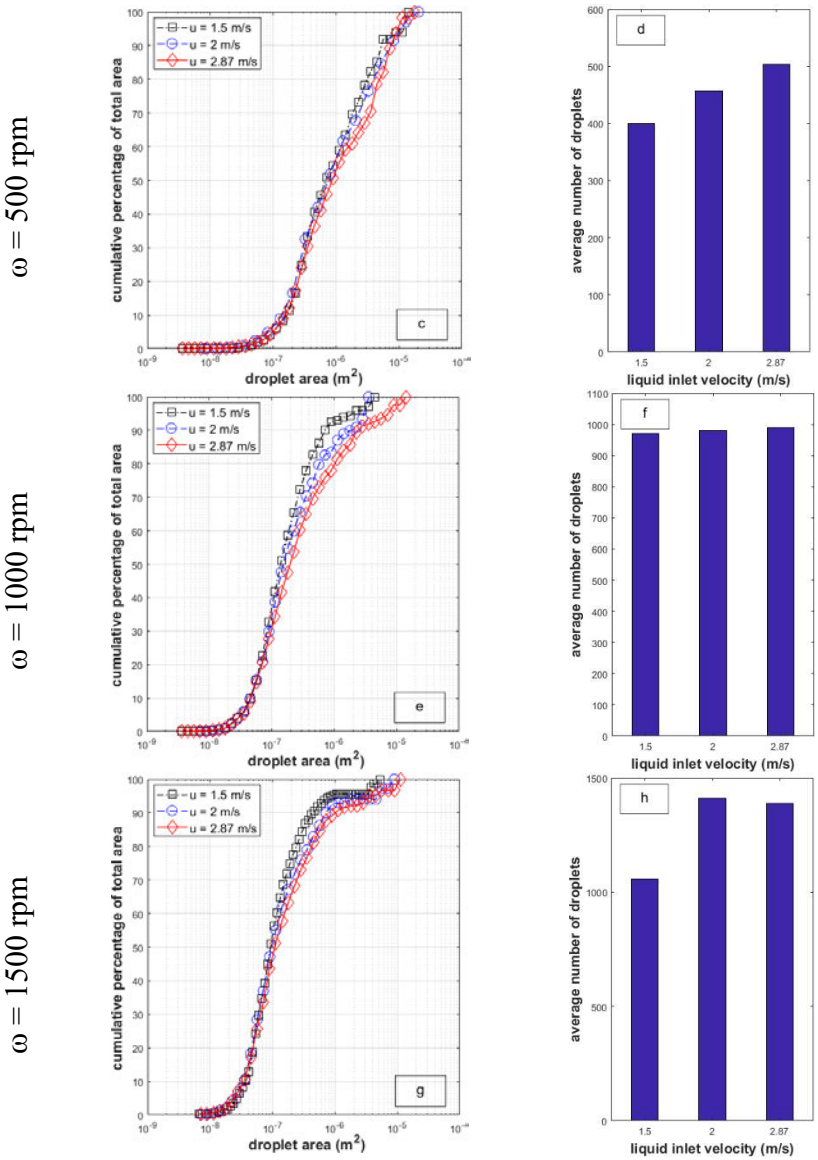

Figure 16. Effect of liquid inlet velocity on the droplet size distribution and average number of droplets at a, b) ω = 250 rpm, c, d) ω = 500 rpm, e, f) ω = 1000 rpm and g, h) ω = 1500 rpm.

3.8. Effect of liquid flow rate

Figure 16 shows the effect of liquid inlet velocity on the droplet size distribution and the average number of droplets. The liquid inlet velocity does not have a significant impact on the droplet size distribution. At larger droplet sizes, however, slight discrepancies can be observed,

which is attributed to the large droplet or broken liquid jet formed after the collision of the main liquid jet and the first layer of wire packing. The average number of droplets also increases slightly with increasing the inlet liquid velocity, as more liquid is being inserted into the bed.

Figure 17 shows the effect of liquid inlet velocity on the average diameter of droplets. As expected from Figures 14 and 15, the average droplet diameter does not change with increasing the inlet liquid velocity. The same trend was observed in previous research on the effect of liquid flow rate [28]. The standard deviation of the droplet size does not change at different liquid flow rates.

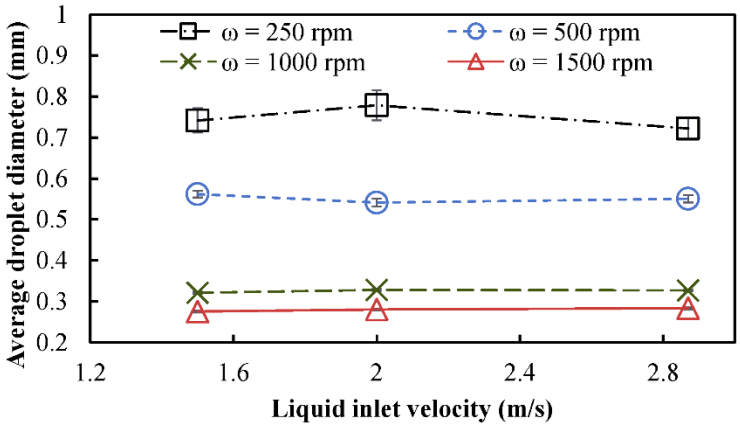

Figure 17. Effect of liquid inlet velocity on the average diameter of droplets.

4. Conclusions

Due to the emission of greenhouse gases, especially CO_2, it is estimated that the average global temperature will increase by 1.5 ± 0.5 ºC before 2050. Rotating packed beds are an efficient and operational solution for enhanced carbon capture in several industries. Despite their brilliant carbon capture efficiency, they are not being utilized commonly, due to their relatively new

technology and complex hydrodynamics. Only during the recent decade with the aid of computational fluid dynamics, researchers could reveal droplet-scale phenomena that occur in these beds. In this article, volume of fluid simulations was utilized to study the hydrodynamics of rotating packed beds. Droplet size distribution, which defines the interfacial area, as a key parameter in RPB design, was investigated. Grid dependency analyses were performed to find the appropriate grid size for each case and the model was validated using experimental data. With increasing rotational speed from 500 rpm to 1500 rpm, finer meshes (100 μm to 50 μm) are required to satisfy grid independence. Furthermore, we investigated the changes in droplet size distribution in two-dimensional and pseudo-three-dimensional cases. It was observed that droplet size distribution does not change in two-dimensional and three-dimensional simulations. This observation unlocks a pathway to investigate larger-scale RPBs with a larger number of grids.

Radial distribution of droplet diameter in the packing region was also studied at different liquid inlet velocities and rotational speeds. It was found that liquid inlet velocity does not have a significant effect, while with increasing rotational speed, the trends of radial distributions of droplet diameter changed. At 250 rpm, the distribution was fluctuating, while at 500 rpm, an increasing-constant trend was observed. With further increasing rotational speed above 1000 rpm, the trend changed to decrease. These trends were explained using a breakup-coalescence model. The breakup and coalescence regimes of droplets during droplet-packing and droplet-droplet collisions depend on the Weber number and impact parameter.

The effects of liquid inlet velocity and rotational speed on the average droplet diameter were studied. It was observed that the average droplet diameter does not change with liquid inlet velocity, while it decreased with increasing rotational speed. The standard deviation of the droplet

diameters also decreased with increasing rotational speed, which means higher uniformity of droplets at high rotational speeds.

Acknowledgement

The authors would like to acknowledge financial support from the Total and Natural Science and Engineering Research Council (NSERC) through the RGPIN-2020-04510 Discovery Grant. Computations were made on supercomputer Cedar and Graham managed by Compute Canada. In particular, the authors would like to acknowledge the efficient support received from Calcul Québec and Compute Canada systems analysts.

Nomenclature

A_d	droplet area, mm^2
A_i	inlet area, m^2
B	distance between the centers of the droplets in a perpendicular plane, m
b	impact parameter, dimensionless
d_1, d_2	diameters of colliding droplets, m
d_d	droplet diameter, m
d_e	packing wire diameter, m
F_σ	continuum surface force, N/m
k	interface curvature, dimensionless
L_{grid}	grid size, μm

Oh	Ohnesorge number, dimensionless
p	pressure, Pa
Q_l	liquid volumetric flow rate, m^3/s
Re	Reynolds number, dimensionless
t	time, s
u_l	liquid superficial velocity at inlet, m/s
u_∞	upstream liquid velocity, m/s
V_r	relative velocity of droplet and packing element, m/s
v	fluid velocity, m/s
We	Weber number, dimensionless
Greek letters	
α	volume fraction, dimensionless
γ	impact angle of droplet and packing element, rad
μ	viscosity, kg/(m·s)
ρ	density, kg/m^3
σ	surface tension, N/m

References

[1] Change, P.C., 2018. Global warming of 1.5° C. *Geneva, Switzerland: World Meteorological Organization*.

[3] Tollefson, J., 2018. IPCC says limiting global warming to 1.5 C will require drastic action. *Nature*, *562*(7726), pp.172-173.

[3] https://climate.nasa.gov/

[4] Ramshaw, C., 1983. Higee' distillation-an example of process intensification. *Chemical Engineer*, pp.13-14.

[5] Ramshaw, C. and Mallinson, R.H., Imperial Chemical Industries Ltd, 1981. *Mass transfer process*. US Patent 4,283,255.

[6] Li, H., Yuan, Z., Liu, Y. and Liu, H., 2019. Characteristics of liquid flow in a countercurrent rotating bed. *Chemical Engineering and Processing-Process Intensification*, *136*, pp.72-81.

[7] Guo, K., Guo, F., Feng, Y., Chen, J., Zheng, C. and Gardner, N.C., 2000. Synchronous visual and RTD study on liquid flow in rotating packed-bed contactor. *Chemical Engineering Science*, *55*(9), pp.1699-1706.

[8] Wu, W., Luo, Y., Chu, G.W., Su, M.J., Cai, Y., Zou, H.K. and Chen, J.F., 2020. Liquid flow behavior in a multiliquid-inlet rotating packed bed reactor with three-dimensional printed packing. *Chemical Engineering Journal*, *386*, p.121537.

[9] Xie, P., Lu, X., Ingham, D., Ma, L. and Pourkashanian, M., 2017. Mass transfer characteristics of the liquid film flow in a rotating packed bed for CO2 capture: A micro-scale CFD analysis. *Energy Procedia*, *142*, pp.3407-3414.

[10] Xie, P., Lu, X., Yang, X., Ingham, D., Ma, L. and Pourkashanian, M., 2017. Characteristics of liquid flow in a rotating packed bed for CO2 capture: A CFD analysis. *Chemical Engineering Science*, *172*, pp.216-229.

[11] Joel, A.S., Wang, M., Ramshaw, C. and Oko, E., 2014. Process analysis of intensified absorber for post-combustion CO2 capture through modelling and simulation. *International journal of greenhouse gas control*, *21*, pp.91-100.

[12] Lin, C.C. and Kuo, Y.W., 2016. Mass transfer performance of rotating packed beds with blade packings in absorption of CO2 into MEA solution. *International Journal of Heat and Mass Transfer*, *97*, pp.712-718.

[13] Zhao, B., Su, Y. and Tao, W., 2014. Mass transfer performance of CO2 capture in rotating packed bed: Dimensionless modeling and intelligent prediction. *Applied energy*, *136*, pp.132-142.

[14] Xue, C.F., Liu, Y.Z. and Jiao, W.Z., 2016. Mass transfer of acrylonitrile wastewater treatment by high gravity air stripping technology. *Desalination and Water Treatment*, *57*(27), pp.12424-12432.

[15] Zeng, Z., Zou, H., Li, X., Arowo, M., Sun, B., Chen, J., Chu, G. and Shao, L., 2013. Degradation of phenol by ozone in the presence of Fenton reagent in a rotating packed bed. *Chemical engineering journal*, *229*, pp.404-411.

[16] Sun, B.C., Wang, X.M., Chen, J.M., Chu, G.W., Chen, J.F. and Shao, L., 2011. Synthesis of nano-CaCO3 by simultaneous absorption of CO2 and NH3 into CaCl2 solution in a rotating packed bed. *Chemical Engineering Journal*, *168*(2), pp.731-736.

[17] Xiuping, L., Youzhi, L., Zhiqiang, L. and Xiaoli, WANG, 2008. Continuous distillation experiment with rotating packed bed. *Chinese journal of chemical engineering*, *16*(4), pp.656-662.

[18] Lin, C.C., Ho, TJ and Liu, W.T., 2002. Distillation in a rotating packed bed. *Journal of chemical engineering of Japan*, *35*(12), pp.1298-1304.

[19] Wen, Z.N., Wu, W., Luo, Y., Zhang, L., Sun, BC and Chu, G.W., 2020. Novel wire mesh packing with controllable cross-sectional area in a rotating packed bed: Mass transfer studies. *Industrial & Engineering Chemistry Research*.

[20] Yang, Y., Xiang, Y., Chu, G., Zou, H., Luo, Y., Arowo, M. and Chen, J.F., 2015. A noninvasive X-ray technique for determination of liquid holdup in a rotating packed bed. *Chemical Engineering Science*, *138*, pp.244-255.

[21] Yang, Y.C., Ouyang, Y., Zhang, N., Yu, QJ and Arowo, M., 2019. A review on computational fluid dynamic simulation for rotating packed beds. *Journal of Chemical Technology & Biotechnology*, *94*(4), pp.1017-1031.

[22] Zhang, W., Xie, P., Li, Y., Teng, L. and Zhu, J., 2020. CFD analysis of the hydrodynamic characteristics in a rotating packed bed with multi-nozzles. *Chemical Engineering and Processing-Process Intensification*, p.108107.

[23] Lu, X., Xie, P., Ingham, D.B., Ma, L. and Pourkashanian, M., 2018. A porous media model for CFD simulations of gas-liquid two-phase flow in rotating packed beds. *Chemical Engineering Science*, *189*, pp.123-134.

[24] Lu, X., Xie, P., Ingham, D.B., Ma, L. and Pourkashanian, M., 2019. Modelling of CO2 absorption in a rotating packed bed using an Eulerian porous media approach. *Chemical Engineering Science*, *199*, pp.302-318.

[25] Xie, P., Lu, X., Ding, H., Yang, X., Ingham, D., Ma, L. and Pourkashanian, M., 2019. A mesoscale 3D CFD analysis of the liquid flow in a rotating packed bed. *Chemical Engineering Science*, *199*, pp.528-545.

[26] Xie, P., Lu, X., Ding, H., Yang, X., Ingham, D., Ma, L. and Pourkashanian, M., 2019. A mesoscale 3D CFD analysis of the liquid flow in a rotating packed bed. *Chemical Engineering Science*, *199*, pp.528-545.

[27] Liu, Y., Luo, Y., Chu, G.W., Larachi, F., Zou, H.K. and Chen, J.F., 2020. Liquid microflow inside the packing of a rotating packed bed reactor: Computational, observational and experimental studies. *Chemical Engineering Journal*, *386*, p.121134.

[28] Liu, Y., Wu, W., Luo, Y., Chu, G.W., Liu, W., Sun, BC and Chen, J.F., 2019. CFD simulation and high-speed photography of liquid flow in the outer cavity zone of a rotating packed bed reactor. *Industrial & Engineering Chemistry Research*, *58*(13), pp.5280-5290.

[29] Liu, W., Luo, Y., Liu, Y.Z. and Chu, G.W., 2020. Scale-Up of a Rotating Packed Bed Reactor with a Mesh-Pin Rotor:(I) Hydrodynamic Studies. *Industrial & Engineering Chemistry Research*, *59*(11), pp.5114-5123.

[30] Liu, W., Luo, Y., Li, YB and Chu, G.W., 2020. Scale-Up of a Rotating Packed Bed Reactor with a Mesh-Pin Rotor:(II) Mass Transfer and Application. *Industrial & Engineering Chemistry Research*, *59*(11), pp.5124-5132.

[31] Yi, F., Zou, H.K., Chu, G.W., Shao, L. and Chen, J.F., 2009. Modeling and experimental studies on absorption of CO2 by Benfield solution in rotating packed bed. *Chemical Engineering Journal*, *145*(3), pp.377-384.

[32] Jasak, H., Jemcov, A. and Tukovic, Z., 2007, September. OpenFOAM: A C++ library for complex physics simulations. In International workshop on coupled methods in numerical dynamics (Vol. 1000, pp. 1-20). IUC Dubrovnik Croatia.

[33] Hirt, C.W. and Nichols, B.D., 1981. Volume of fluid (VOF) method for the dynamics of free boundaries. Journal of computational physics, 39(1), pp.201-225.

[34] Brackbill, J.U., Kothe, D.B. and Zemach, C., 1992. A continuum method for modeling surface tension. *Journal of computational physics*, *100*(2), pp.335-354.

[35] Yan, Z.Y., Lin, C. and Ruan, Q., 2014. Dynamics of droplets and mass transfer in a rotating packed bed. *AIChE Journal*, *60*(7), pp.2705-2723.

[36] Rygg, J.R., 2013. *CFD analysis of a Pelton turbine in openFOAM* (Master's thesis, Institutt for energi-og prosessteknikk).

[37] Jain, M., Prakash, R.S., Tomar, G. and Ravikrishna, R.V., 2015. Secondary breakup of a drop at moderate Weber numbers. *Proceedings of the Royal Society A: Mathematical, Physical and Engineering Sciences*, *471*(2177), p.20140930.

[38] Yang, B. and Chen, S., 2018. Simulation of interaction between a freely moving solid particle and a freely moving liquid droplet by lattice Boltzmann method. *International Journal of Heat and Mass Transfer*, *127*, pp.474-484.

[39] Saroka, M.D. and Ashgriz, N., 2015. Separation Criteria for Off-Axis Binary Drop Collisions. *Journal of Fluids*, *2015*.

[40] Chen, Y., DeMauro, E.P., Wagner, J.L., Arienti, M., Guildenbecher, D.R., Farias, P., Grasser, T.W., Sanderson, P., Albert, S., Turpin, A. and Sealy, W., 2017. Aerodynamic breakup and secondary drop formation for a liquid metal column in a shock-induced cross-flow. In *55th AIAA Aerospace Sciences Meeting* (p. 1892).

[41] Pawar, S., Padding, J., Deen, N., Jongsma, A., Innings, F. and Kuipers, J.H., 2015. Numerical and experimental investigation of induced flow and droplet–droplet interactions in a liquid spray. *Chemical Engineering Science*, *138*, pp.17-30.

[42] Kozak, P. and Asztalos, K., 2015. Effects of Liquid Droplet-Droplet Interactions in a Pressure Swirl Spray.

[43] Mundo, C.H.R., Sommerfeld, M. and Tropea, C., 1995. Droplet-wall collisions: experimental studies of the deformation and breakup process. International journal of multiphase flow, 21(2), pp.151-173.

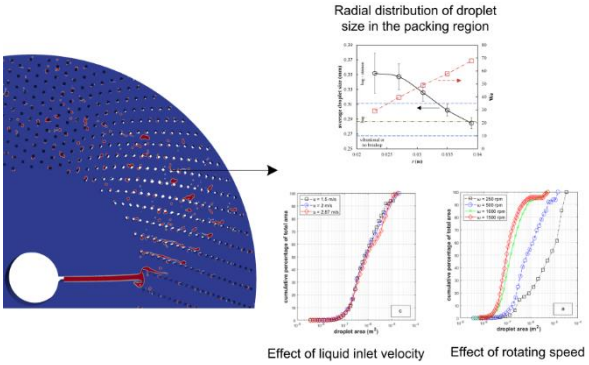

Abstract graphics